

Local heat transfer in rotating square-rib-roughened and smooth channels with jet impingement

Shou-Shing Hsieh^{*}, Huang-Hsiu Tsai, Shih-Chi Chan

Department of Mechanical and Electro-Mechanical Engineering, National Sun Yat-Sen University, Kaohsiung 80424, Taiwan, ROC

Received 14 March 2003; received in revised form 23 October 2003

Abstract

An experimental investigation was carried out to examine the effects of jet impinging positions on heat transfer from rib-roughened (square and semi-circular) channels with rotational speeds of up to 600 rpm. The rib height (e) was fixed at 1.5 mm and pitch-to-height ratio (p/e) kept at 6.67. The study covered jet Reynolds number in the range 5000–9000 based on jet hole diameter. Results were presented for rotational number, jet impinging positions, and roughened surfaces effects on local Nusselt numbers. Significant heat transfer enhancement was found for the present physical geometry and within the ranges of operating parameters considered in the study. Moreover, detailed heat transfer coefficients on target wall in a rotating square smooth channel using transient liquid crystal techniques for the rotational speeds of 30 and 60 rpm at $Re_j = 7000$ and 9000 were also examined.

© 2004 Elsevier Ltd. All rights reserved.

1. Introduction

Jet impingement cooling has long been an area of active research, and with an ever increasing scope of application, the field continues to attract plenty of attention. Effective turbine cooling is necessary to enhance to efficiency of advanced aircraft engines. Consequently, jet impingement cooling becomes an important application in this area [1,2]. In addition, rotation of a cooling passage gives rise to Coriolis and buoyancy forces that can significantly alter the local heat transfer in the inward/outward coolant passage [3].

Extended surfaces enhance convective heat transfer in many applications through both an increase in the convective surface area and the modification of the heat transfer coefficient due to the increased flow turbulence [4,5]. As mentioned earlier, most studies concentrated on jets impinging on smooth, flat surfaces. However, the new studies of jet impingement combined with roughened surfaces have generally promising results [6,7].

Recently, the transient liquid crystal (TLC) technique has been widely used in many areas. Chyu et al. [8] examined heat transfer performance of multiple delta wings using a transient liquid crystal technique. Hwang and Cheng [9] experimentally studied the local heat transfer coefficients and static wall pressure drops in leading-edge triangular ducts cooled by wall/impinged jets by using transient liquid crystal technique. However, such techniques (TLC) seem not to have been applied to impingement jet in a rotating channel. Only Taslim et al. [10] reported a TLC study for internal cooling passage heat transfer measurements at rotating speeds about 50–200 rpm.

Based on the literature review with rotation, it is found that, in addition to the aspect ratio, the ratio of wall temperature to local fluid temperature, and which wall is heated, the local Nusselt number in the flow direction of the impingement of a confined air jet on a constant heat flux roughened flat plate is a function of following variables and it can be written in the following form:

$$Nu = Nu(Re_j, Re_\Omega, H/d, x/d, e/D_h, p/e, q) \quad (1)$$

in which H/d is jet-to-wall spacing, q stands for surface heat flux, x is the flow direction, and d is jet hole diameter. Re_j is the jet Reynolds number based on hole

^{*} Corresponding author. Tel.: +886-7-525-2000x4215; fax: +886-7-525-4215.

E-mail address: sshsieh@mail.nsysu.edu.tw (S.-S. Hsieh).

Nomenclature

| | | | |
|-------------|--|--------------------------------|--|
| A | area of heated surface | T_j | jet exit temperature, K |
| C_p | constant pressure specific heat, kJ/kg K | $T_{b,x}$ | local bulk mean fluid temperature, K |
| D_h | hydraulic diameter of the channel, mm | $T_{w,x}$ | local wall temperature, K |
| d | jet hole diameter (= 2 mm) | u_j | average jet exit velocity, m/s |
| e | roughness height, mm | W | width of the channel, mm |
| H | jet-to-wall spacing (= 10 mm) | w | width of the roughness element, mm |
| G | mass flow rate, kg/s | X | dimensionless lateral distance, x/d |
| H/d | dimensionless jet-to-wall spacing | x | lateral distance from the midpoint of the test section, mm |
| h_x | local convective heat transfer coefficient, $q/(T_{wx} - T_{bx})$, W/m ² K | Y | dimensionless spanwise distance, y/d |
| k | thermal conductivity of air, W/m K | y | spanwise distance, mm |
| L | test section length (= 200 mm) | | |
| ℓ | transverse length of the roughness element, mm | <i>Greek symbols</i> | |
| Nu | local Nusselt number, $h_x d_j / k$ | α | thermal diffusivity, m ² /s |
| p | pitch of the roughness element, mm | ν | kinematic viscosity at T_j , m ² /s |
| Q | total heat flux, W | ρ | density of fluid, kg/m ³ |
| Q_{cv} | corrected heat flux from Eq. (5), W | Ω | rotational speed, rpm |
| q | surface heat flux, Q_{cv}/A | <i>Subscripts/superscripts</i> | |
| R | rotating radius, mm | j | jet |
| r_Ω | rotating arm length (= 150 mm) | s | spanwise |
| Re_j | jet Reynolds number, $u_j d / \nu$ | x | local downstream position |
| Re_Ω | rotational Reynolds number based on the rotating radius, $\Omega R^2 / \nu$ | w | wall/surface |
| | | – | average |
| | | Ω | rotation |

diameter, $v_j d / \nu$ and Re_Ω is the rotational Reynolds number based on the rotational speed Ω and the rotating radius R . D_h is the hydraulic diameter of the channel, e/D_h is the relative height of roughness, and p/e is the roughness density.

In this work an experimental study of the heat transfer of a single circular air jet on heated rotating roughened walls was studied for Re_j from 5000 to 9000, $H/d = 5$, and Re_Ω from 0 to 600 rpm with a constant heat flux level of 1596 W/m². In addition to the thermocouple temperature measurements, detailed heat transfer coefficients on the target wall of a smooth rotating square duct are also measured by using transient liquid crystal techniques. Temperature measurements for the target were made to quantitatively determine the local heat transfer coefficients under various Re_j and Re_Ω and different surface conditions. While TLC measurements were conducted to determine the detailed heat transfer coefficients for impingement cooling in a rotating square smooth channel, Tables 1 and 2 give the relevant parameters of the present study for thermocouple and TLC measurements, respectively.

The objectives of the study are fourfold: (1) to apply the experimental method developed to the acquisition of local data for heat transfer between a rotating roughened channel and impinging jet; (2) to explore the effects

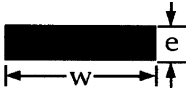
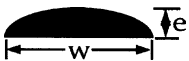
of Re_j , Re_Ω , roughness types, and flow impingement onto the roughness element positions on local heat transfer characteristics in a single circular jet with rotation; (3) to broaden our fundamental understanding of the confined circular jet impinging on roughened surfaces with rotation; and (4) to examine the possibility for jet impingement cooling measurements in a rotating channel using TLC techniques.

2. Experiment

2.1. Experimental apparatus and procedure for roughened channels

The experimental setup and channel details for temperature measurement are shown in Fig. 1. The facility is mainly comprised of a test section, a compressor, a motor, a power supply, two slip ring assemblies, and a data logger, which is quite similar to that of Hsieh et al. [11] except for a modification for roughened test surface. The hollow rotating shaft in Fig. 2 is driven by 1 HP DC motor via a toothed belt drive pulley system through a frequency-controlled motor controller with a maximum rotating speed of 1600 rpm. The rotational speed is measured by a digital photo tachometer. The rotating

Table 1
Test section geometries and operation conditions for thermocouple measurement

| Geometries of ribs | W (mm) | e (mm) | l (mm) | p (mm) | D_h | p/e | D_h/d | e/D_h |
|---|----------|----------|----------|----------|-------|-------|---------|---------|
|  | 3 | 1.5 | 10 | 10 | 9.20 | 6.67 | 4.60 | 0.163 |
|  | 3 | 1.5 | 10 | 10 | 9.42 | 6.67 | 4.71 | 0.159 |

| Geometries of test section | | | | | | | |
|----------------------------|----------|----------|------------|----------|-----------------|-----------|--|
| W (mm) | H (mm) | L (mm) | $L/2$ (mm) | d (mm) | r_Ω (mm) | $AR(H/W)$ | |
| 10 | 10 | 200 | 100 | 2 | 150 | 1 | |

Relevant parameters

$$Re_j = 5000\text{--}9000$$

$$Ro = \frac{Re_\Omega}{Re_j} = 0\text{--}0.0032 \text{ (0–600 rpm)}$$

Test section boundary conditions

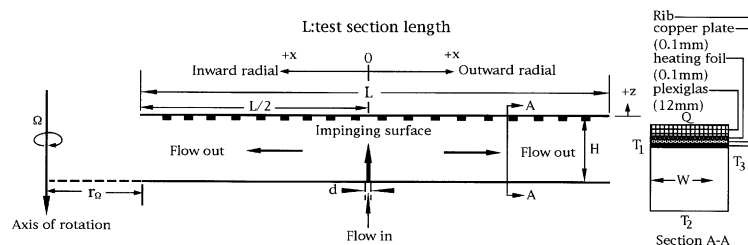
$$Q = \text{constant heat flux } (1596 \pm 76 \text{ W/m}^2)$$

$$T_1 = T_2 = T_3 = \text{isothermal } (27 \text{ }^\circ\text{C})$$

Impinging position

At the center of two consecutive ribs (type A)

At the top of the rib (type B)



shaft and supporting bearing system are mounted on a rigid, heavy steel plate. The rotating channel mounted on a disk which is connected perpendicularly to the rotating shaft. The impinging air jet with an average velocity at exit about 39.2–70.6 m/s issuing from the hole (nozzle) is supplied by a high-pressure compressor system and stored in a 200 l air tank for eliminating air pressure fluctuation. Air flow rate is controlled and measured by a precise pressure regulator (model FCK-500) and compensated for the temperature effect. A flexible tube at the end of the air supply system is connected to the air jet chamber, which is composed of two air plenums. The upper plenum is made of 12 mm thick plexiglas which is 200 mm long and the internal cross section is 10×10 mm. The details of the test section assembly are also presented in Fig. 2.

The main part was a strip of 0.1 mm thick copper plate with a heating section of nominal 176×13 mm etched thin-foil heater with a thickness of 0.15 mm exposed to the coolant to warrant a nearly uniform heat

flux hold. The test section consisted of a square channel with a cross section of 10×10 mm mounted on a shaft supported by two bearings. The airjets generated from the air jet chamber impinge normally onto the center of a heated impingement block. The heated impingement surface is 176 mm long, 13 mm wide, 12.2 mm thick and composed of three layers (see Section A-A in Table 1 for details). The first layer is the heated impingement surface, made of a 0.1 mm thick copper plates with a size of 176×13 mm. It is polished to minimize the surface emissivity. Therefore, it reduces radiative heat losses. The second layer is a 170×12 mm etched thin-foil heater with a thickness of 0.1 mm, cemented onto the backside of the first layer. The etched thin-foil heater, which can be applied to a voltage up to 60 V, was attached on the copper plates. The third layer (i.e. outer layer) is 12 mm thick plexiglas, which is adhered to the backside of the film heater to prevent conductive heat losses from the heaters. The maximum possible heat flux is 0.15 MW/m².

Table 2
Test section geometries and operation conditions for TLC measurement

| Geometries of test section | | | | | | |
|----------------------------|----------|----------|------------|----------|-----------------|-----------|
| W (mm) | H (mm) | L (mm) | $L/2$ (mm) | d (mm) | r_Ω (mm) | $AR(H/W)$ |
| 10 | 10 | 200 | 100 | 1 | 150 | 1 |

Relevant parameters
 $Re_j = 7000\text{--}9000$ $Re_\Omega = 0.367$ $Ro = \frac{Re_\Omega}{Re_j} = 0.000052$ (rotational number)

Test section boundary condition
 T_∞ = heated air temperature
 $T_1 = T_2 = T_3 = T_4$ = isothermal (27 °C)

Sixteen square and semi-circle type repeated roughness elements (1.5 mm high) made of copper are glued on the copper surface with $p/e = 6.67$. The layer of glue between the roughness element and the copper plates is thin enough so that the thermal resistance is negligible. The spacing between ribs is 10 mm. The temperature of the center of the inner surface (exposed to the flow) of the heater was measured by 17 gage 40-Fe-Cn thermocouples which were electrically insulated from the thin-foil heater. The spanwise spacing of any two neighboring thermocouples is 10 mm. The thermocouples were spring-loaded against the copper surface and a silicone paste (cement) was applied to each thermocouple bead to provide electrical isolation but with good thermal contact. The impingement surface is designed to provide a known heat flux and also to measure the wall temperature at various locations. Teflon strips, 1.59 mm thick, function as dividers are machined along the periphery of each copper plate for insulation. Temperatures measured at the center of bottom surface of the copper plates were used with a solution of the two-dimensional heat equation to obtain the temperature field within the plate and the distribution of the convection heat transfer coefficient along the impingement surface. A two-dimensional conduction model was used to provide wall temperature correction estimates for the measurements.

The strip on either side of the active section was connected to plexiglas bus blocks, which were in turn con-

nected to power leads. The jet nozzle is inserted in a balsa wood plate with a jet hole length to jet diameter of $t/d = 0.75$ which serves as a jet plate and is 1.5 mm thick. The jet direction relative to rotation axis is in parallel, but exit flow (wall jet) direction is perpendicular to the rotation axis. To reduce the heat loss from the jet plate, it is also covered with 12 mm thickness plexiglas (not shown), which ensures that the impingement plate and the jet plate are insulated. The assembly was fixed in a stainless steel frame with flange screwed to the rotating disk. The power source was an autotransformer, supplied from a standard 110 V, 60 Hz AC wall outlet, and designed for a load output of 20, 40, and 60 V with a maximum current of 3 A. The power to the heating foils is measured by an accurate digital power meter. Two additional thermocouples are used to measure the bulk fluid temperature at the inlet/exit. All the temperature signals are acquired with a data logger (YEW Model 3088) and sent into a 586 PC for data processing and plotting.

2.2. Experiments for smooth channel (TLC measurements)

2.2.1. Test apparatus

The experimental apparatus includes a flow circuit, thermochromatic liquid crystal imaging test section, and instruments, which is schematically shown in Fig. 2. Compressed air was blown through a flow meter, that

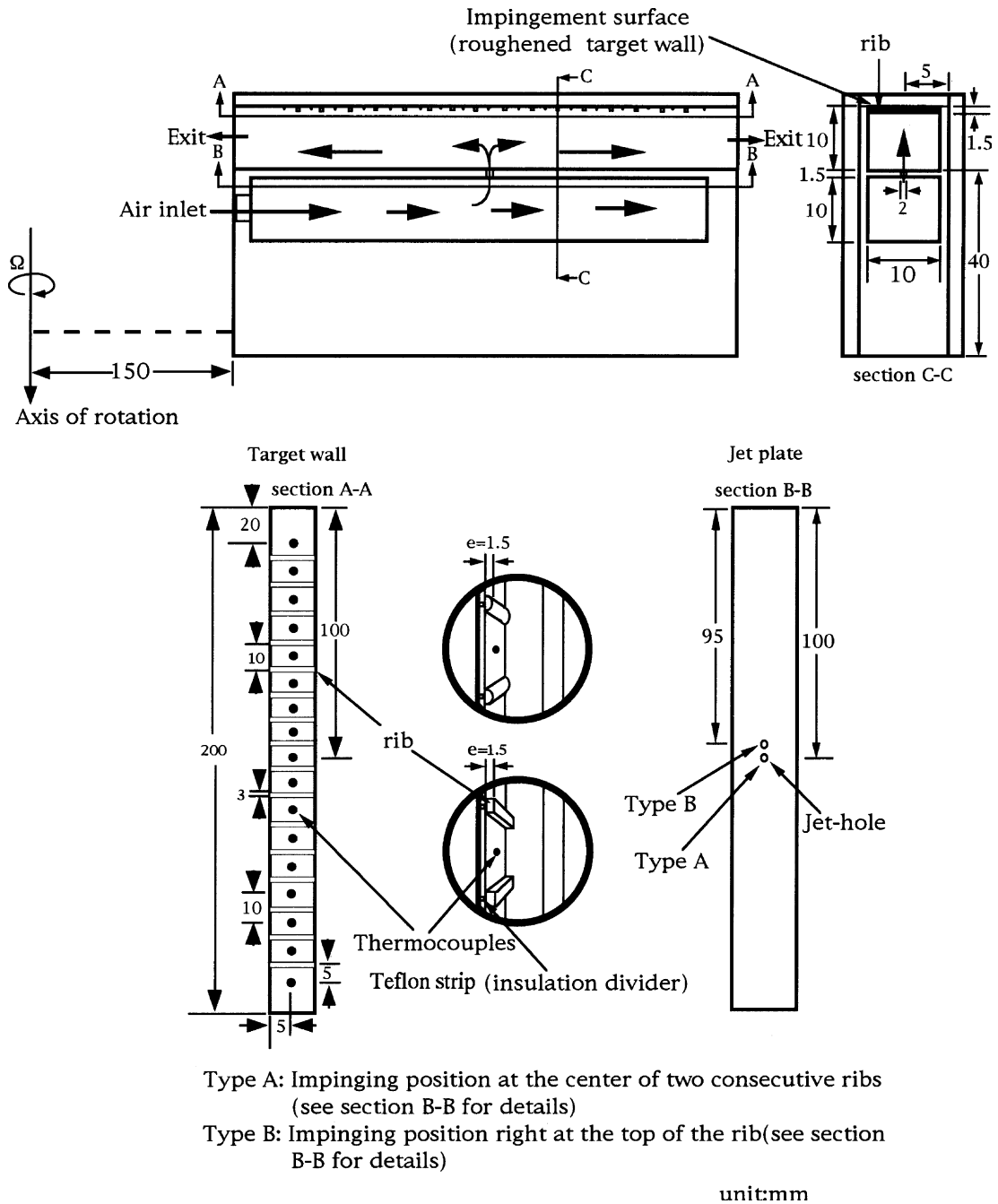


Fig. 1. Detailed dimensions of the test section.

measures the volumetric flow rate of the airflow, and then flows into an electric heater to be heated to a required temperature. A 16 mm × 16 mm × 26 mm CMOS camera (model: MO-S616G) with a light source directly facing the nozzle exit, and mounted on the rotating arm was used to record the color change of the liquid crystal coating as the heated airflow passed through test section

and, then impinged through the nozzle onto the target wall. Two thermocouples (Type TT-T-40-1000) located at the test section inlet and outlet, as also shown in Fig. 2, respectively are connected to a real-time temperature recorder (YOKOGAWA, MV 100) to measure the mainflow temperature history, as shown in Fig. 3 at the upstream and downstream locations of the test section.

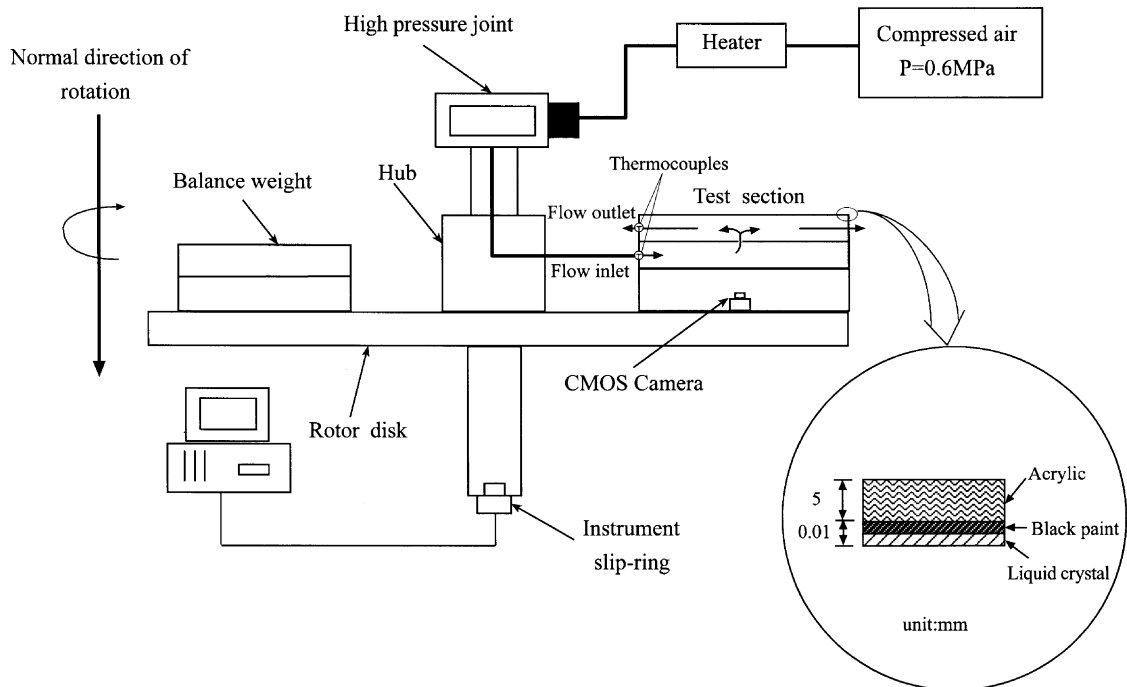


Fig. 2. Experimental setup and instrumentation.

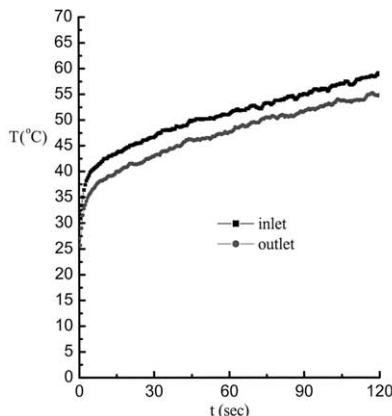


Fig. 3. Mainstream temperature variations during the transient test.

The time of color change of the liquid crystals during a transient test is measured by a Sony 1/3" color CMOS sensor and a computer vision system. The target surface is airsprayed with black background paints first and then liquid crystal (Hallcrest, BM/R40C5W/C17-10) of thickness of the order of 10 μm . Besides, a CMOS camera, a frame grabber interface associated with Pentium III PC was used to analyze the color changes using a commercial image processing software (LCIA, Taiwan Pitot Co.). The image processing system maps the test section into 320×240 pixels locations and monitors each

location individually for color change. Since the reflected light from liquid crystals is dependent on the spectral intensity of the incident light and contains a peak value whose wavelength inversely depends on the temperature [12], great care was taken to ensure the CMOS attachment. The test section is shielded from room light and room air currents using a thick black felt curtain covered in such way that the target walls only receive incident light emitted from the light source mounted inside the CMOS.

The light source used for this series of tests is a standard 60 mm Taiwan Concept cool white fluorescent lamp (13 W NB4210-60 mm). The typical cool white fluorescent has a color temperature of 4100 K and a spectral distribution that is high in the yellow-green range. In order to reduce the UV radiation damage to transient liquid crystals, a spectrum EB-74 UV sleeve filter was used to obtain 100% UV blockage. A lens with an extended view angle of 92° was implemented with the present CMOS camera to minimize angle effects and to achieve uniform illumination intensity throughout the domain of measured.

2.3. Analysis of liquid crystal thermography and experimental procedure

The local heat transfer coefficient over the target wall can be obtained by assuming one-dimensional transient conduction over a semi-infinite solid wall with the initial

and boundary conditions on the liquid crystal coated surfaces. It can be estimated by the following:

$$\rho_s C_{ps} \frac{\partial T}{\partial t} = k \frac{\partial^2 T}{\partial z^2} \quad (2)$$

$$T = T_i \quad \text{at } t = 0 \quad \text{and } z \geq 0$$

$$k \frac{\partial T}{\partial z} = h(T_w - T_\infty) \quad \text{at } z = 0$$

$$T = T_i \quad \text{as } t \rightarrow \infty$$

This gives the dimensionless wall temperature response as follows:

$$\frac{T_w - T_i}{T_\infty - T_i} = 1 - \exp\left(-\frac{h^2 \alpha t}{k^2}\right) \operatorname{erfc}\left(\frac{h\sqrt{\alpha t}}{k}\right) \quad (3)$$

Once T_i (up to 27 °C), T_∞ (~60 °C), and the corresponding time (t) required to change the coated-surface color to green are known, the heat transfer coefficient h can be estimated from Eq. (3). The green color of the liquid crystal shows the largest light intensity, which is a reference point that conventionally uses. Noting that in Eq. (3), the original T_∞ is a constant. However, in the present study, T_∞ is time-dependent and increases as the time (t) increases (see Fig. 3 for temperature history) which can be simulated as a series of step functions. Applying the Duhamel's superposition principle, Eq. (3) can be rewritten in the following:

$$T_w - T_i = \sum_{j=1}^N \left[1 - \exp\left(-\frac{h^2 \alpha (t - \tau_j)}{k^2}\right) \times \operatorname{erfc}\left(\frac{h(\sqrt{\alpha(t - \tau_j)})}{k}\right) \right] (\Delta T_\infty) \quad (4)$$

where T_∞ and τ_j are the temperature and time step changes from the recorder readout. Since the time duration is too short to make the heat transport to the plexiglas plate, the assumption of the semi-infinite solid wall as stated before was assessed.

During the tests, the liquid crystal is initially colorless at room temperature (about 27 °C) and then it changes to red, green, blue, and finally colorless again. The total temperature change of the liquid crystal is about 5 °C (40–45 °C) for the color changes. The time for the color change is about 120–180 s for the cases under study. Actually, it depends on the location, mainstream temperature, and airflow rate. The color change temperatures to red, green and blue are 40, 41, and 45 °C, respectively.

Once the test section including target surface coated with liquid crystals has been set up, tests were conducted by suddenly exposing the hot air to the test section. This results in a color change of the surface coating. Before each test, the test section was kept at the laboratory ambient temperature (~27 °C). Positioned directly over

the target walls is a three-chip Sony CCD camera. Each image is captured as a three-dimensional matrix of red, green, and blue values. The image size is 320 × 240 × 3 (≅0.22 MB). Image processing begins with a captured image for the entire target walls which is 320 × 240 pixels. During the experiments, the image processing system records the time for the color change to green for the entire surface. Finally, the time and temperature are keyed in a computer program to obtain the local heat transfer coefficient.

3. Data reduction

For estimating the convective heat flux dissipated from the heated impingement plate, based on the energy balance, it is proposed that at steady state, the local heat generated by the thin-foil heater Q_i is converted into the following heat transfer modes during the experiments: (1) conductive heat loss, Q_c ; (2) radiative heat loss, Q_r ; and (3) convective heat dissipated from the impingement plate, Q_{cv} . That is,

$$Q_{cv} = Q_i - Q_c - Q_r \quad (5)$$

This energy balance of Eq. (5) calculates the net convective heat, Q_{cv} , dissipated from the impingement plate to the air jet in the confinement. Heat loss calculations were obtained with no coolant flow (i.e. no jet impingement) with the channel ends sealed and the internal recirculation was restricted as well and constant electrical power was supplied under steady-state conditions with rotation. The total power input to heater is Q_i which equals $I^2 R$. Here I is the electric current of the AC power supply and R is the resistance of the thin-foil heater. It was verified in preliminary tests that the variation of resistance with temperature could be neglected (less than 0.2%), as the heater temperature variation was less than 40 K in the present study and the variation in resistivity with temperature is extremely small. Q_r is the radiative heat loss from the copper surface to its surroundings. It is calculated using thermal diffuse gray-body networks. Based on the above analysis, the maximum radiative heat loss is less than 5% of the total power input for all the cases under study. Q_c is the conductive heat loss to the copper plate and balsa block and was calculated using a two-dimensional conduction model and, eventually, to the room through the plexiglas. It is found that Q_c value varies from 5% to 20% of the total input power.

Before the experiments, all the thermocouples are calibrated in a constant temperature bath to ensure the measurement accuracy of ±0.1 °C. In each test run, the mass flow rate is adjusted to give the desired Reynolds number. After steady state is reached, the temperature distribution on the test plate is measured. It usually takes 30 min to reach steady state except for the first

data set. To get the local Nusselt number, one uses the following equation:

$$h_x = \frac{Q_{cv}}{A(T_{w,x} - T_{b,x})} \quad (6)$$

$$T_{b,x} = T_j + Q_{cv}/GC_p \quad (7)$$

The area A of the heated surface was carefully measured for each test section. The value of $T_{b,x}$ is obtained by an energy balance. The local Nusselt number is defined in terms of jet hole diameter as $Nu_x = h_x d_j / k$. Experimental data were taken in both rotating and stationary channels. Rotational speeds of 60, 120, 180, 240, 300, 360, 420, and 600 rpm were set in a clockwise direction.

4. Uncertainty estimates

The uncertainty in the measurement can be categorized into three parts. The first is from the mass flow rate, the second is due to the convective heat transfer

Table 3
Maximum possible errors for TLC measurements

| Quality | Systematic error (%) | Random error (%) |
|------------|----------------------|------------------|
| L | ± 0.15 | ± 0.003 |
| W | ± 0.15 | ± 0.05 |
| H | ± 0.15 | ± 0.05 |
| d_j | ± 0.15 | ± 0.50 |
| A_j | ± 0.17 | ± 0.71 |
| A | ± 0.17 | ± 0.05 |
| t | ± 0.17 | ± 0.42 |
| Re_j | ± 1.01 | ± 1.25 |
| T_∞ | ± 0.41 | ± 0.83 |
| T_w | ± 0.41 | ± 1.22 |
| T_i | ± 0.41 | ± 1.85 |
| α | ± 0.71 | ± 0.93 |
| k | ± 0.50 | ± 0.53 |
| h | ± 1.13 | ± 2.63 |
| Nu | ± 1.25 | ± 2.73 |

coefficient, and the third is for detailed heat transfer coefficients by using TLC techniques. The first is caused by the flow meter. The jet temperatures were measured

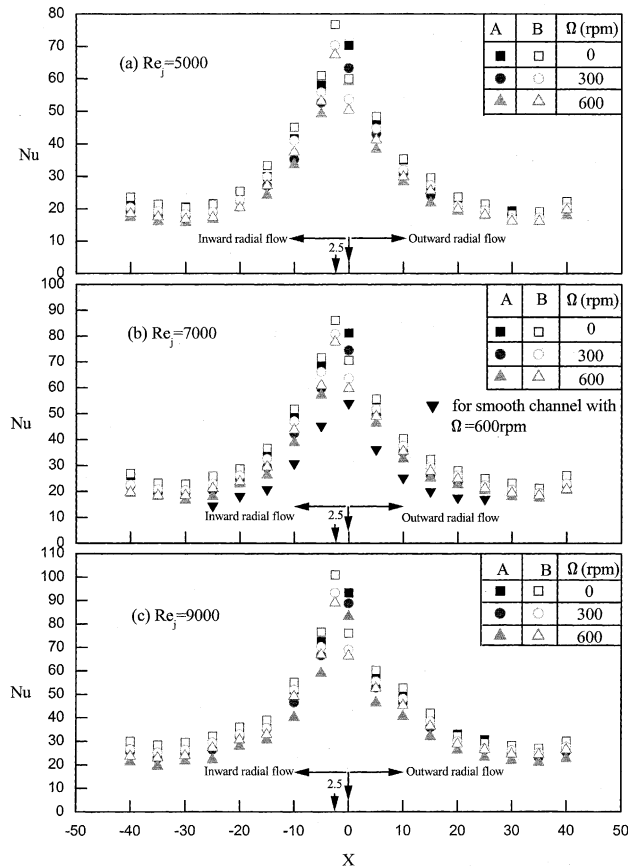


Fig. 4. Combined effect of rotation and impinging position on the axial variation of local Nusselt number for square ribs.

just upstream of the nozzle inlet and were maintained at 25 ± 0.1 °C throughout the thermocouple temperature measurements (not for TLC measurements). Jet flow rates were measured upstream of the plena using a floating meter (HC Model P-23-41G) which was accurate to within 1% of full-scale (0.5 l/s). The inlet Prandtl number was $0.7 (\pm 0.5\%)$ based on the jet exit temperature. The flow rates were used to determine mean nozzle discharge velocities from which impingement velocities were calculated. The uncertainty in Nusselt number was influenced primarily by the determination of heat flux and wall temperature. The heat flux was corrected, followed by Eq. (5). The determination of the heated impingement wall temperature was related to the thermal resistance of the adhesive layer (~ 0.1 mm) between the thermocouple bead and bottom wall of the copper plate. Since the thermal resistance of the adhesive layer is extremely small (typical value; 7×10^{-10} m² K W⁻¹), the uncertainty was determined to be negligible (4.9×10^{-6} °C). The uncertainty in Reynolds number was affected by measurement of the flow rate and the nozzle exit area. Based on the above uncertainty estimate [13],

the uncertainty in Re_j was 6.2% and the Nusselt number was found to be less than 9.5%.

For TLC measurements, the measurement variance, geometry uncertainty and calibration errors for the transient time, green-point temperature and thermal-physical property of the wall (e.g. k and α) are estimated. As stated before, the conduction heat losses can be negligible due to quite a short transient time and the low thermal conductivity of the insulation for TLC measurements. Moreover, thermal radiation is relatively small because of a nearly uniform wall temperature for the present study. Table 3 summarizes the estimate of maximum inaccuracy (system error) and imprecision (random error) associated with each measurement.

5. Results and discussion

Streamwise heat transfer coefficients for jet plate configurations summarized in Table 1 was presented and discussed in the following. The present objectives are to examine the heat transfer coefficients as a function of the

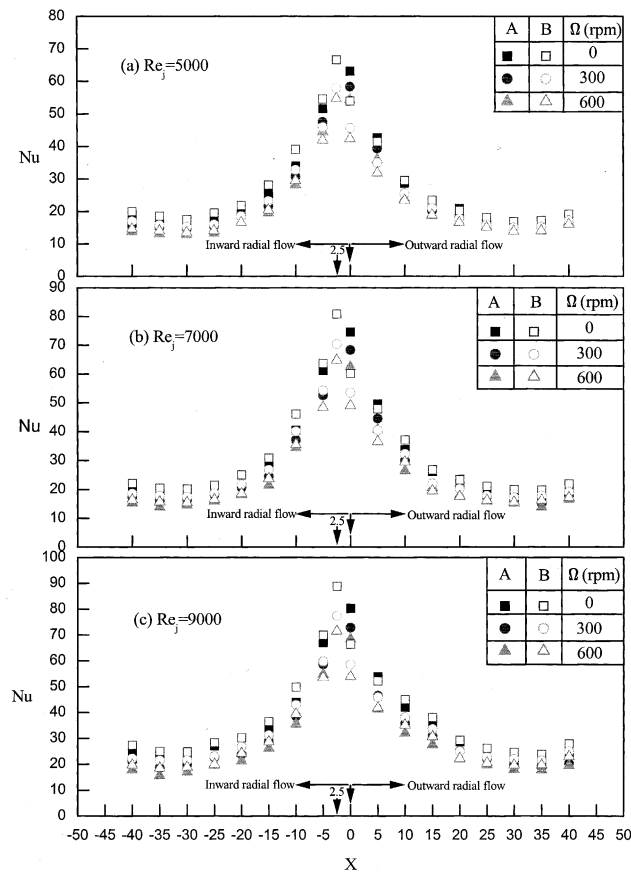


Fig. 5. Combined effect of rotation and impinging position on the axial variation of local Nusselt number for semi-circular ribs.

associated spanwise jet velocity, rotational speed, and geometric parameters such as roughness element geometry, and jet impingement positions. For a channel of $Pr = 0.72$, $H/d = 5$, rotating mean radius ($= 350$ mm), and definite q , the Nusselt number can be expressed as a function of Re_j , Re_Ω , x/d , p/e , e/D_h . Air properties are calculated based on $(T_j + T_w)/2$. Detailed heat transfer coefficients were also determined for impingement cooling in a square smooth channel of rotational speeds of 30 and 60 rpm at $Re_j = 7000$ and 9000.

5.1. Combined effect of rotation and impingement position (offset and types A and B)

For combined effect of rotation and impingement position with different jet exit velocity, the present results shown in Fig. 4(a)–(c) seem to show a definite trend. The open symbol indicates that the jet impinging position is 2.5 mm offset to the original, also type B arrangement and namely, the jet is impinging onto the middle of the two consecutive roughness elements.

While, for type A, there is no offset, i.e., the jet is directly head on the rib. In fact, Fig. 4(a) shows that the effect of rotation on heat transfer with roughness elements is clearly noted. There is an significant influence on Nu with/without rotation for square ribs as shown in Fig. 4(a) where Nu decreases as Ω increases. Such a situation gradually increased as Re_j increases which can be seen from Fig. 4(b) and (c). Furthermore, Fig. 4(b) with an increase in Re_j , rotational effect seems reactivated and consequently, Nu has a lower value in Fig. 4(b) as Re_Ω increases due to centrifugal and Coriolis forces. Obviously, flow distribution seems only slightly more complex than those without rotation. Offset has an influence with a higher stagnation heat transfer coefficient on Nu among these figures shown. The same situation happens for the semi-circular rib as shown in Fig. 5.

Figs. 6 and 7 (no impingement position offset) show the results of rotating channel with different rib geometry for type A and B arrangements. Two types of roughness element (rib and semi-circular) were used. It is

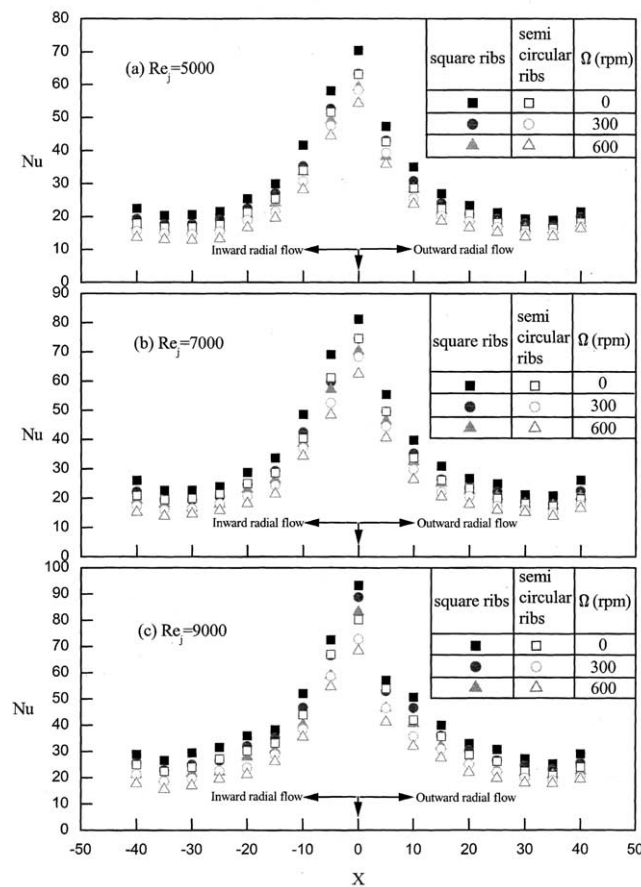


Fig. 6. Combined effect of rotation and geometry of ribs on the axial variation of local Nusselt number for type A.

found that local Nu of the rib type roughness is consistently highly than that of semi-circular rib for both types A and B arrangements.

For impingement cooling over a rib-roughened wall, the protrusion of the ribs has the effect of promoting turbulence in the wall jet region. In addition, the wall jet can separate from the rib, reattach to the bottom, and recirculate inside the cavity. As evident from previous study, for instance, Hansen and Webb [14], the heat transfer is strongly dependent on the interaction of the following three possible factors: (1) the level of local turbulence, (2) the fluid velocity at the surface, and (3) the percentage of surface area exposed to normal impingement. Based on the primary mechanisms through which rib-roughened surfaces affect the heat transfer coefficient for impinging air jets, Figs. 6 and 7 clearly indicate that the different rib-roughened surfaces do have a noticeable enhancement. Both roughness elements do show an enhancement effect of 20% or more as compared to those of smooth channels, for instance, as shown in Fig. 4(b). The major reason can be attributed to the

interaction of three factors stated above. In addition, the traditional bell-shape like curve still preserves.

5.2. Combined effect of rotation, impingement position, and rib geometry

Fig. 8 shows the combined effects of rotation, rib-roughened types, and the impingement positions on the local Nusselt number ratio; Nu_r/Nu_s , $Nu_{r,s}/Nu_{r,s,c}$, and $Nu_{r,B}/Nu_{r,A}$. Here $Nu_{r,s,c}$ stands for the local Nu for a semi-circular rib surface with rotation; while $Nu_{r,s}$ is for a square roughened surface. Note that the Nusselt number ratio in each plot of Fig. 8 is the local Nusselt number with rotation, roughened surfaces, and impingement positions effect divided by its corresponding measured local Nusselt number for non-rotation, roughened surface, and impingement position, respectively, under the same conditions. Actually, Fig. 8(a)–(c) superimposed the separated plots of Nu_r , $Nu_{r,s}$, $Nu_{r,B}$ and $Nu_{r,A}$ on the corresponding plots of Nu vs. X . Among these results, Fig. 8(a) indicates the enhancement factors

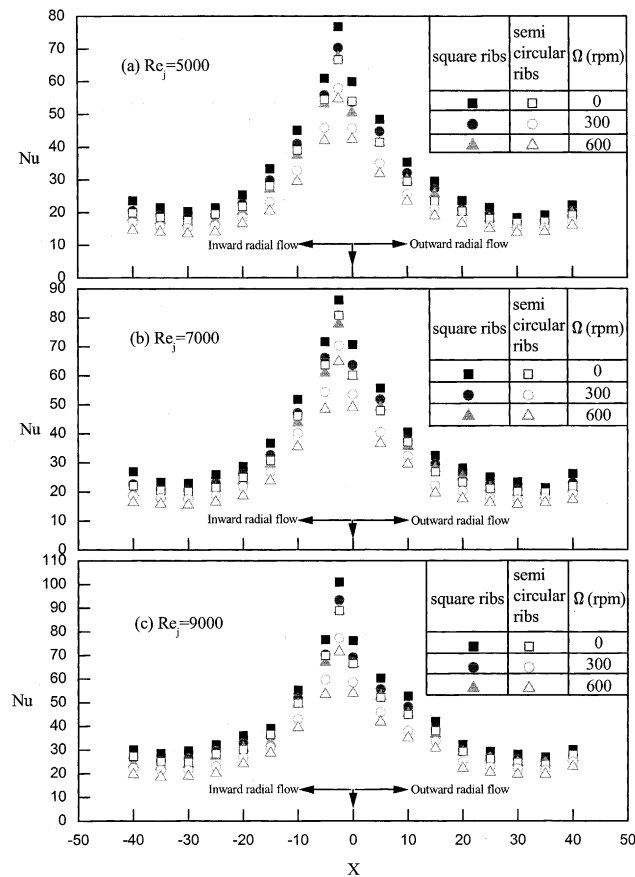


Fig. 7. Combined effect of rotation and ribbed surface on the axial variation of local Nusselt number for type B.

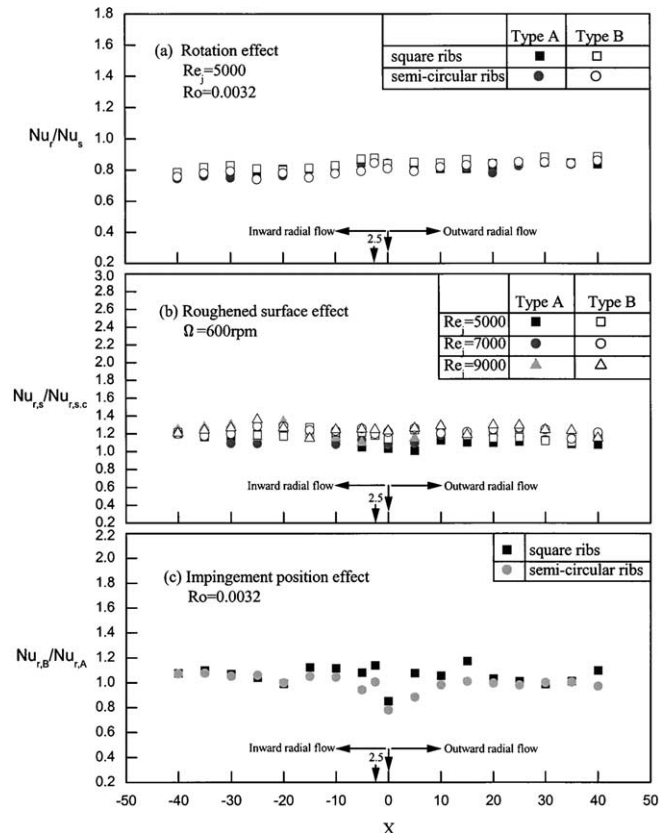


Fig. 8. Effect of rotation, impingement position and geometric of ribs on the axial variation of local Nusselt number.

less than 1 with rotating channel for the cases studied herein at $Ro = 0.0032$. The data show that the Nu ratio distribution begins at 0.8 with a slow and gradual rise to a peak of 0.9 at stagnation point and, then, gradually decreases to a constant value 0.85 for type A and B rib arrangement, respectively. Fig. 8(b) illustrates the sole effect due to roughened surfaces. The enhancement factor can be up to 1.4 at $\Omega = 600$ rpm and $X = -25$ for type B rib arrangement at $Re_j = 9000$. The distributions start at stagnation with a slow decrease and then, followed by a slight drop and, finally, increase monotonically to a value of 1.2 along downstream at $\Omega = 600$ rpm and $X = 40$. Fig. 8(c) shows that the impingement position destroys the symmetry about the nozzle exit plane by shifting the jets. This results in an increase in downstream heat transfer from the stagnation point. Nu at stagnation for type A has the highest value as compared to that of type B. This would give the relative value at this point below 1.

5.3. Detailed Nusselt number contours

It has long been recognized that the flow pattern of impinging jets from single round nozzles shown above

can be subdivided into three characteristic regions: the confined jet region, the stagnation flow region, and the region of lateral flow outside the stagnation zone, also termed the wall jet region of which they can also be identified in Figs. 9 and 10. Generally, three regions could be clearly seen. Axisymmetric structures are present near the jet hole (nozzle) exit. These structures typically grow and pair into larger structures until they impinge the target wall. Although entrainment has diluted the starting vortex, it still appears to be fairly symmetric for a stationary channel (Fig. 9(a)). Wall jet regions to the far left and right of the impinging jets appear green with weak brightness ($X \cong \pm 10$).

Fig. 9(a)–(c) show the detailed distribution of dimensionless local heat transfer coefficient, Nu on the target wall. TLC measurements were made from $-10 \leq X \leq 10$. There are 4 or 5 color zones over the entire surfaces as seen from the color contours. The detailed Nusselt number contour indicates that the heat transfer performance is noticeably affected by the rotation from the brightness of the color and the areas of the color changes. Furthermore, due to the different flow phenomena occurrence caused by the effect of induced centrifugal force and Coriolis force/or their combination

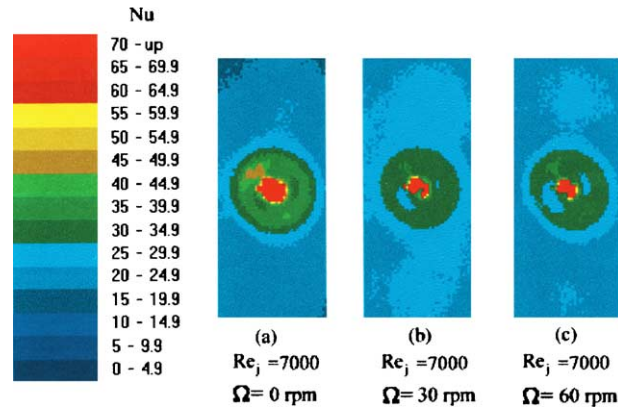


Fig. 9. Detailed heat transfer distribution for smooth channel and different rotational speed at $Re_j = 7000$.

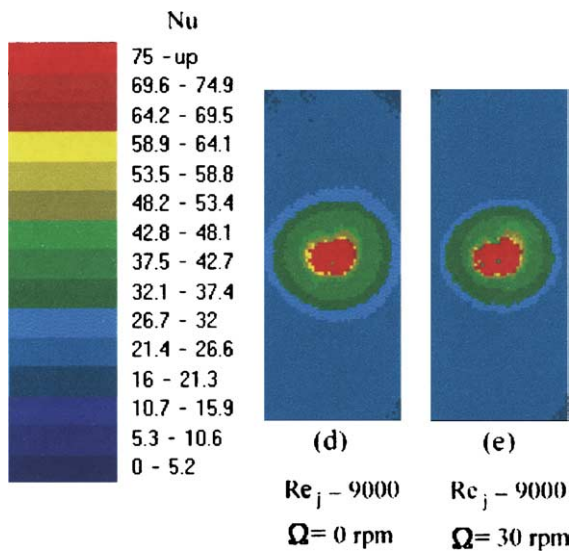


Fig. 10. Detailed heat transfer distribution for smooth channel and different rotational speed at $Re_j = 9000$.

in radially out/inward channels (positive/negative x direction), the detailed Nu contour showed a little bit unsymmetric behavior as one compares Fig. 9(a) with those of Fig. 9(b) and (c).

The detailed Nusselt number contour indicates that the entrance effect is clearly seen for Fig. 9(a) for a stationary case. The Nusselt number decreases a bit as the rotational speed increases. However, Nu increases as Re_j increases. The heat transfer coefficients are high on the center region of the channel because the forced velocities are large. Due to the present rotational channel, there is Coriolis force in the lateral direction due to exit jet flow which generated the secondary flow in the cross section of the channel perpendicular to the radially in/outward direction. Moreover, the centrifugal force is now in the radially outward direction. Such effect de-

creases as Re_j increases. The behavior is quite similar to that of Hsieh et al. [11]. Regarding $Re_j = 9000$, as shown in Fig. 10, the detailed Nu contours are somewhat different from the corresponding contours for $Re_j = 7000$. The wall jet effect for $Re_j = 9000$ obviously is more significant than that for $Re_j = 7000$ because the penetration depth of the wall jet on the target wall is deeper for $Re_j = 9000$ for both $\Omega = 0$ and 30 rpm (see Fig. 9(a) and (b)). This also confirmed by this fact that the areas of poor heat transfer along the wall jet downstream reduces. In summary, based on Figs. 9 and 10, for the detailed heat transfer coefficients, the jet exits from the hole and impinges onto the target wall at the corresponding location (i.e. stagnation point) that produces round zones (red areas in Figs. 9 and 10) of high heat transfer. The wall jet boundary layer thickness along the target surface is gradually increased as the flow develops in the radial in/outward direction. On the target surface, high heat transfer areas are also gradually reduced as the rotational speed increases. Simultaneously, the region of poor heat transfer on the target wall is gradually increases downstream.

5.4. Local Nusselt number (at $Y = 0$ and ± 2.5), span-averaged Nusselt number and area-averaged Nusselt number

The local convective heat transfer coefficient can be found using Eq. (6), and the local Nusselt number is defined in term of the jet hole diameter as before; i.e.,

$$Nu = \frac{h_x d}{k} \tag{8}$$

The general feature again shows that Nu of bell shape with the highest at the stagnation point, where local Nusselt numbers agree, and then drops off in the wall jet region with increasing x/d and the heat transfer

coefficients increase with increasing Re_j due to the occurrence of a thinner thermal boundary layer. The variation of the local Nusselt number with x distance at

the midplane (i.e. $y = W/2$) for different rotational speeds is shown in Fig. 11 at $Re_j = 7000$, for all the cases (i.e., $0 \leq \Omega \leq 60$ rpm), the maximum Nusselt number is

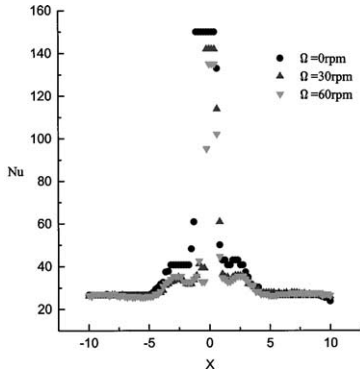


Fig. 11. Local Nusselt number vs. X for smooth channel at $Re_j = 7000$ under different rotational speed.

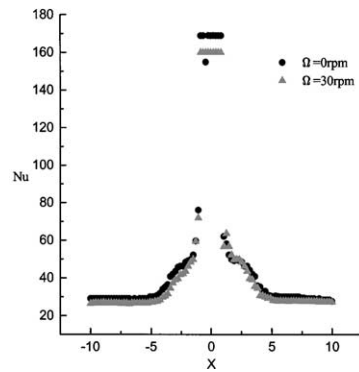


Fig. 12. Local Nusselt number vs. X for smooth channel at $Re_j = 9000$ under different rotational speed.

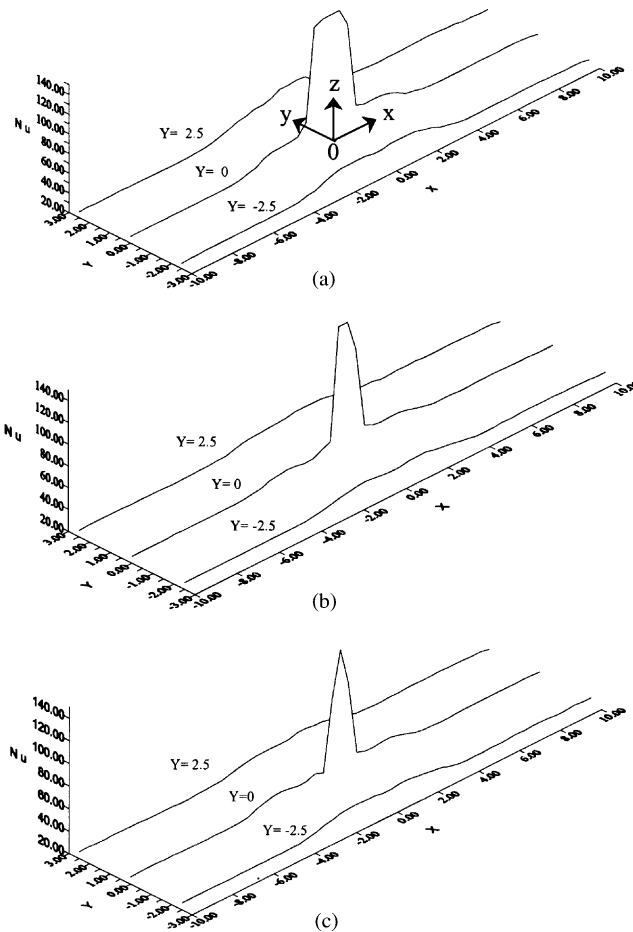


Fig. 13. Nu distribution at $Y = \pm 2.5$ at $Re_j = 7000$ for smooth channel and different rotational speed: (a) $\Omega = 0$ rpm, (b) $\Omega = 30$ rpm, and (c) $\Omega = 60$ rpm.

at the stagnation point. The higher rotational speed is, the lower Nu has. The peak shifts from $X = 0$ to ± 2 are due to the uncertainty in interpretation of the transient liquid crystal measurement results caused by a “saturation” of the present measurement procedure. The same trend was found for $Re_j = 9000$ except for a high value of Nu as expected, which is shown in Fig. 12. From Figs. 11 and 12, it is found that the decrease in Nusselt number is gradual for jets with a high rotational number but increase sharply for a higher Re_j . Figs. 13 and 14 further show that the Nu distribution at $Y = \pm 2.5$ for different rotational speeds at $Re_j = 7000$ and 9000 , respectively. Again, the bell shape like Figs. 13 and 14 is still hold. However, mid-span distance becomes smaller as Re_j and rotational speed increases. As a result, the influence zone of the present impingement jet seems not as large as one expected. Namely, the 3-D effect (including Y direction effect) of the present jet seems insignificant for both Re_j s at all the rotational speeds under study. This is perhaps because the jet momentum in the span direction (Y -direction) is reduced from $Y = 0$. Figs. 15 and 16 show the variation of span-averaged Nusselt number \overline{Nu}_s for $Re_j = 7000$ and 9000 , respectively. Again, the same tendency with a smoother distribution was found. The trend showed that rotation did not significantly change Nusselt number distribution, but decreased Nusselt number values slightly. This is the same as stated in Hsieh et al. [11] because the rotation induced centrifugal force causes the jets to bend

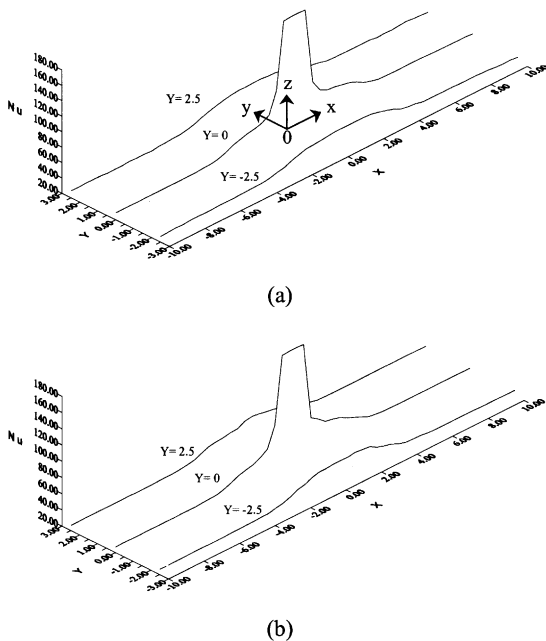


Fig. 14. Nu distribution at $Y = \pm 2.5$ at $Re_j = 9000$ for smooth channel and different rotational speed: (a) $\Omega = 0$ rpm and (b) $\Omega = 30$ rpm.

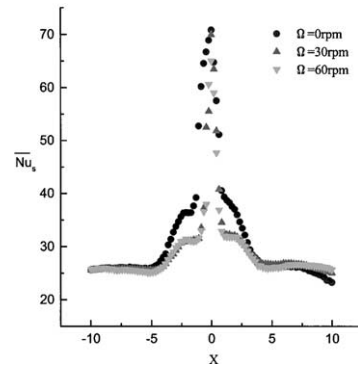


Fig. 15. Spanwise average Nusselt number vs. X for smooth channel at $Re_j = 7000$ under different rotational speed.

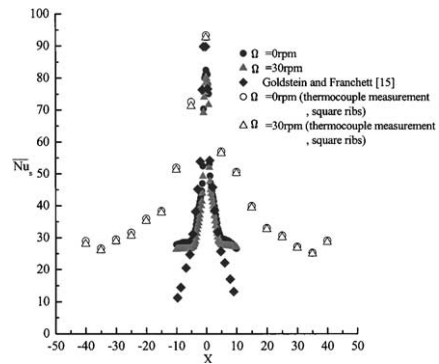


Fig. 16. The comparison of spanwise average Nusselt number vs. X for smooth channel at $Re_j = 9000$ under different rotational speed.

and deflect away from the target walls and, consequently, reduces the impingement effect on target walls. It appears that the bending and deflection jets due to rotation induced centrifugal force would result in a lower impingement effect on the target walls. Therefore, lower heat transfer values were recorded as shown in Figs. 13–16. So Figs. 9 and 10 do. Also included in Fig. 16 is the results ($Re_j = 10,000$; $H/d = 4$) from Goldstein and Franchett [15] for comparison. The difference in magnitude is expected because the jet hole size and jet-to-wall spacing as well as operating conditions are totally different. Besides, the stationary (non-rotating) thermocouple measurement results for the present roughened channel are also included. The results of the present roughened channels are higher than those of TLC measurements as one would expect.

Moreover, taking a closeup examination, Nusselt number values in the radially outward channel (positive x direction) have slightly different from their correspondence in radially inward channel (negative x direction). In fact, the former was found about 5% higher than that of the latter at a same Re_j . Such unsymmetric

behavior can also be seen from the detailed Nusselt number contours as stated before. In fact, a peak point of Nu shift was found in Hsieh et al. [11] may explain the above unsymmetric behavior for this study. However, such shifts may not be clearly observed due to a relative low rotational speed of the present study. In addition, the effect of Re_j on heat transfer from Figs. 13–16 in the study is clearly noted again even though only two cases ($Re_j = 7000$ and 9000) were considered.

6. Conclusion

The paper presents a study of experimental data from heat transfer experiments for impingement cooling in rotating roughened rectangular channels. Important results were obtained. Rotation as well as roughness types seems to have an influence on heat transfer. For rotation, heat transfer performance was lower as compared to that of without rotation. The heat transfer would increase up to 20–30% for the present roughness types. The enhancement for square rib roughened type is higher than that of semi-circular type. Furthermore, the present detailed heat transfer coefficient measurements has made it possible to examine for the first time the possibility of TLC technique employed to the impingement cooling measurements in a rotating square smooth channel. In spite of the low rotational speeds, the data and techniques may still be helpful for documentation as well as measurement skill promotion in this regard.

References

- [1] K.V. Akella, J.C. Han, Impingement cooling in rotating two-pass rectangular channels with ribbed walls, *J. Thermophys. Heat Transfer* 13 (3) (1999) 364–371.
- [2] D.E. Metzger, L.D. Grochowsky, Heat transfer between an impinging jet and rotating disk, *ASME J. Heat Transfer* 99 (1977) 663–667.
- [3] S.-S. Hsieh, Y.J. Hong, Heat transfer coefficients in an orthogonal rotating duct with turbulators, *ASME J. Heat Transfer* 117 (1995) 69–78.
- [4] J.C. Han, Heat transfer and friction characteristics in rectangular channels with rib turbulators, *ASME J. Heat Transfer* 110 (1988) 321–328.
- [5] Y.J. Hong, S.-S. Hsieh, Heat transfer and friction factor measurements in ducts with staggered and in-line ribs, *ASME J. Heat Transfer* 115 (1993) 28–65.
- [6] C. Gau, C.C. Lee, Impingement cooling flow structure and heat transfer along rib-roughened walls, *Int. J. Heat Mass Transfer* (1992).
- [7] D. Priedeman, V. Challehan, B.W. Webb, Enhanced of liquid jet impingement heat transfer with surface modification, *ASME J. Heat Transfer* 116 (1994) 486–489.
- [8] M.K. Chyu, H. Ding, J.P. Downs, A. Van Sutendael, F.O. Soechting, Determination of local heat transfer coefficient based on bulk mean temperature using a transient liquid technique, *ASME Paper*, NO. 97-GT-489, 1997.
- [9] J.-J. Hwang, C.-S. Cheng, Impingement cooling in triangular ducts using an array of side-entry wall jets, *Int. J. Heat Mass Transfer* 44 (2001) 1053–1063.
- [10] M.E. Taslim, A. Rahman, S.D. Spring, Experimental investigation of heat transfer coefficients in a spanwise rotating channel with two opposite rib-roughened walls, *ASME J. Turbomach.* 113 (1991) 75–82.
- [11] S.-S. Hsieh, J.-T. Huang, C.-F. Liu, Local heat transfer in a rotating square channel with jet impingement, *ASME J. Heat Transfer* 121 (1999) 811–818.
- [12] J.W. Baughn, M.R. Anderson, J.E. Mayhew, J.D. Wolf, Hysteresis of thermo-chronic liquid crystal temperature measurement based on hue, *ASME J. Heat Transfer* 121 (1999) 1067–1072.
- [13] S.J. Kline, F.A. McClintock, Describing uncertainty in single simple experiments, *Mech. Eng. (Am. Soc. Mech. Eng.)* 75 (1953) 3–8.
- [14] L.G. Hansen, B.W. Webb, Air jet impingement heat transfer from modified surfaces, *ASME J. Heat Transfer* 36 (1993) 989–997.
- [15] R.J. Goldstein, M.E. Franchett, Heat transfer from a flat surface to an oblique impinging jet, *ASME J. Heat Transfer* 110 (1988) 84–90.